

Scattering properties of the $2e^-2e^+$ polyelectronic system

K. M. Daily,¹ Javier von Stecher,² and Chris H. Greene¹

¹*Department of Physics, Purdue University, West Lafayette, Indiana 47907, USA*

²*Seagate Technology, Longmont, Colorado 80503, USA*

(Dated: January 26, 2022)

We study the $2e^-2e^+$ equal-mass charge-neutral four-body system in the adiabatic hyperspherical framework. The lowest few adiabatic potentials are calculated for zero orbital angular momentum, positive parity, and charge conjugation symmetries. Propagating the R -matrix, the low-energy s -wave scattering lengths of the singlet-singlet and triplet-triplet spin configurations are calculated. Lastly, we calculate the S -matrix for energies above the ionic threshold to estimate the transition rates between the single ionic fragmentation channel and the lowest few dimer-dimer fragmentation channels.

PACS numbers:

I. INTRODUCTION

Many charged few-body systems have been studied using the hyperspherical framework. From Macek's pioneering work [1], the three-body Coulomb problem has been extensively studied [2–8] and reviewed (see Refs. [5, 9] and references within). There have been notable studies of four-body charged systems as well [10–12], and even a first look at the equal-mass five-body system [13].

An interesting class of charged systems is that of particle-antiparticle mixtures [14]. These systems are inherently unstable due to annihilation, but are fundamental, e.g., the high rates of Ps annihilation at the galactic bulge [15] or precision tests of CPT violation via anti-hydrogen [14, 16]. Moreover, there have been many advancements towards a gamma-ray laser based on the development of a BEC of spin-polarized Ps [17–21] and the experimental observation of the Ps₂ molecule [22].

Using the adiabatic hyperspherical framework [23, 24], we examine the $2e^-2e^+$ equal-mass charge-neutral four-body system. The adiabatic Hamiltonian is solved utilizing a basis of explicitly correlated Gaussians at a fixed hyperradius [25–27]. The evaluation of matrix elements is facilitated using a Fourier transform technique [13]. The hyperradial R -matrix is propagated and the low-energy s -wave scattering lengths are calculated. Also, from the S -matrix we estimate the transition probabilities between the ionic channel and the lowest few Ps₂ dimer-dimer channels.

The rest of the paper is organized as follows. Section II defines the Hamiltonian and the basis set used to solve the adiabatic Hamiltonian. Section III analyzes the adiabatic potential curves, that is, the solutions to the adiabatic Hamiltonian. Section IV describes how the low-energy elastic scattering lengths are calculated and compares the results to benchmark calculations from the literature. In Sec. V, the S -matrix is calculated to estimate the transition probabilities between the lowest few dimer-dimer fragmentation channels and the single ionic fragmentation channel. Last, Sec. VI concludes.

II. THEORETICAL BACKGROUND

Consider the system of two electrons and two positrons in three dimensions interacting via the two-body Coulomb potential. The Hamiltonian H in atomic units ($\hbar = m_e = 1$) reads

$$H = -\frac{1}{2} \sum_{j=1}^4 \nabla_{\mathbf{r}_j}^2 + \sum_{i<j} \frac{q_i q_j}{|\mathbf{r}_i - \mathbf{r}_j|} \quad (1)$$

where \mathbf{r}_j is the location of particle j . For concreteness, $q_1 = q_2 = +1$ and $q_3 = q_4 = -1$. The center of mass H_{CM} and relative H_{rel} contributions separate, $H = H_{\text{CM}} + H_{\text{rel}}$. Our focus is on the relative Hamiltonian,

$$H_{\text{rel}} = -\frac{1}{2\mu} \sum_{j=1}^3 \nabla_{\boldsymbol{\rho}_j}^2 + V_C(\boldsymbol{\rho}_1, \boldsymbol{\rho}_2, \boldsymbol{\rho}_3), \quad (2)$$

where V_C contains the pair-wise Coulomb interactions as a function of the three relative Jacobi vectors $\boldsymbol{\rho}_j$, $j = 1, 2, 3$. All Jacobi vectors are scaled such that they are analogous to three equal-mass “particles” of mass μ . We take $\mu = 2^{-2/3}$ such that the coordinate transformation is unitary.

The relative Hamiltonian H_{rel} is recast in hyperspherical coordinates in terms of eight hyperangles denoted by $\boldsymbol{\Omega}$ and a single length, the hyperradius R . The relative Hamiltonian is then a sum of the hyperradial kinetic energy \mathcal{T}_R , the hyperangular kinetic energy $\mathcal{T}_{\boldsymbol{\Omega}}$, and the interaction potential,

$$H_{\text{rel}} = \mathcal{T}_R + \mathcal{T}_{\boldsymbol{\Omega}} + V_{\text{int}}(R, \boldsymbol{\Omega}), \quad (3)$$

where

$$\mathcal{T}_R = -\frac{1}{2\mu} \frac{1}{R^8} \frac{\partial}{\partial R} R^8 \frac{\partial}{\partial R}. \quad (4)$$

The exact form of the hyperangular kinetic energy $\mathcal{T}_{\boldsymbol{\Omega}}$ depends on the choices of the Jacobi vectors and of the hyperangles. The exact form is not needed here, but additional detail can be found in Ref [24].

The solution $\Psi_E(R, \mathbf{\Omega})$ to Eq. (3) is expanded in terms of the radial functions $R^{-4}F_{E\nu}(R)$ and the channel functions $\Phi_\nu(R; \mathbf{\Omega})$,

$$\Psi_E(R, \mathbf{\Omega}) = R^{-4} \sum_{\nu} F_{E\nu}(R) \Phi_\nu(R; \mathbf{\Omega}). \quad (5)$$

The channel functions at a fixed hyperradius R form a complete orthonormal set over the hyperangles,

$$\int d\mathbf{\Omega} \Phi_\nu^*(R; \mathbf{\Omega}) \Phi_{\nu'}(R; \mathbf{\Omega}) = \delta_{\nu\nu'}, \quad (6)$$

and are the solutions to the adiabatic Hamiltonian $H_{\text{ad}}(R, \mathbf{\Omega})$,

$$H_{\text{ad}}(R, \mathbf{\Omega}) \Phi_\nu(R; \mathbf{\Omega}) = U_\nu(R) \Phi_\nu(R; \mathbf{\Omega}), \quad (7)$$

where

$$H_{\text{ad}} = \frac{\mathbf{\Lambda}^2 + 12}{2\mu R^2} + \frac{C(\mathbf{\Omega})}{R}. \quad (8)$$

Here, $\mathbf{\Lambda}^2$ is the square of the grand angular momentum operator and $C(\mathbf{\Omega})$ is the hyperangular part of the Coulomb interaction.

After applying Eq. (3) on the expansion Eq. (5) and projecting from the left onto the channel functions, the Schrödinger equation reads

$$\begin{aligned} & \left(-\frac{1}{2\mu} \frac{d^2}{dR^2} + U_\nu(R) - E \right) F_{E\nu}(R) \\ & - \frac{1}{2\mu} \sum_{\nu'} \left(2P_{\nu\nu'}(R) \frac{d}{dR} + Q_{\nu\nu'}(R) \right) F_{E\nu'}(R) = 0. \end{aligned} \quad (9)$$

The hyperspherical Schrödinger equation Eq. (9) is solved in a two step procedure. First, $H_{\text{ad}}(R, \mathbf{\Omega})$ is solved parametrically in R for the adiabatic potential curves $U_\nu(R)$. In a second step, the coupled set of one-dimensional equations in R are solved. In Eq. (9), $P_{\nu\nu'}$ and $Q_{\nu\nu'}$ represent the coupling between channels, where

$$P_{\nu\nu'}(R) = \left\langle \Phi_\nu \left| \frac{\partial \Phi_{\nu'}}{\partial R} \right\rangle_{\mathbf{\Omega}} \quad (10)$$

and

$$Q_{\nu\nu'}(R) = \left\langle \Phi_\nu \left| \frac{\partial^2 \Phi_{\nu'}}{\partial R^2} \right\rangle_{\mathbf{\Omega}}. \quad (11)$$

The brackets indicate that the integrals are taken only over the hyperangle $\mathbf{\Omega}$ with the hyperradius R held fixed.

The eigenfunctions $\Phi_\nu(R; \mathbf{\Omega})$ of $H_{\text{ad}}(R, \mathbf{\Omega})$ are simultaneous eigenstates of the total orbital angular momentum L , the parity π , and the spin of the identical positrons S_+ and identical electrons S_- . Moreover, because of the equal masses and charges, the eigenfunctions are also eigenstates of the charge conjugation operator \hat{C} . The $\Phi_\nu(R; \mathbf{\Omega})$ are expanded using a non-orthogonal basis of correlated Gaussians [25–27],

$$|\Phi_\nu\rangle = \sum_j \hat{C}_\pm \hat{S} |A^{(j)}\rangle |\chi\rangle, \quad (12)$$

TABLE I: Permutations used in the basis functions Eq. (12) labeled by the charge conjugation and spin. SS (TT) means singlet-singlet (triplet-triplet).

	C_+ SS	C_+ TT	C_- SS	C_- TT
1	+	+	+	+
(12)	+	–	+	–
(34)	+	–	+	–
(12)(34)	+	+	+	+
(13)(24)	+	+	–	–
(3142)	+	–	–	+
(1324)	+	–	–	+
(14)(23)	+	+	–	–

where \hat{S} is a symmetrization operator that permutes the space and spin labels of identical particles. In particular, $\hat{S} = [1 - (12)][1 - (34)]$, where (ij) is the two-cycle operator that exchanges particles i and j . The three-cycle operator (ijk) , for example, denotes the permutation $i \rightarrow j$, $j \rightarrow k$, and $k \rightarrow i$. In practice, to project out the parts of the functions that are either even (+) or odd (–) under charge conjugation, we apply the operator \hat{C}_\pm , $\hat{C}_\pm = 1 \pm \hat{C}$, where $\hat{C} = (13)(24)$.

In general, under permutation the spin functions $|\chi\rangle$ would transform to a different spin configuration. However, this work only considers the singlet-singlet (SS) or triplet-triplet (TT) spin configurations. In this case, the effect of permutations on the spin functions leaves them unchanged except possibly for an overall minus sign. The combined operator $\hat{C}_\pm \hat{S}$ involves eight permutations. Table I indicates all of the permutations and their effective signs that are considered in this work. The first column denotes the permutation while the first row denotes the system considered.

The functions $|A^{(j)}\rangle$ are

$$|A^{(j)}\rangle = \exp\left(-\frac{1}{2} \mathbf{x}^T \underline{A}^{(j)} \mathbf{x}\right) |\mathbf{u}^T \mathbf{x}|^{2K}. \quad (13)$$

Here, \mathbf{x} is an array of (column) Jacobi vectors, $\mathbf{x}^T = \{\mathbf{x}_1, \mathbf{x}_2, \dots, \mathbf{x}_N\}$. All Jacobi vectors exist in three dimensions, such that the j^{th} Jacobi vector reads $\mathbf{x}_j^T = \{x_{j,1}, x_{j,2}, x_{j,3}\}$. $\underline{A}^{(j)}$ is an $N \times N$ symmetric positive definite coefficient matrix that describe the correlations. The matrix $\underline{A}^{(j)}$ contains $N(N+1)/2$ independent variational parameters. The N -dimensional global vector \mathbf{u} determines the linear combination of Jacobi vectors, where the integer K is a nodal parameter. These basis functions describe only natural parity states [$\pi = (-1)^L$] with zero orbital angular momentum L , though it is well-known how to extend this basis to include unnatural parity [27].

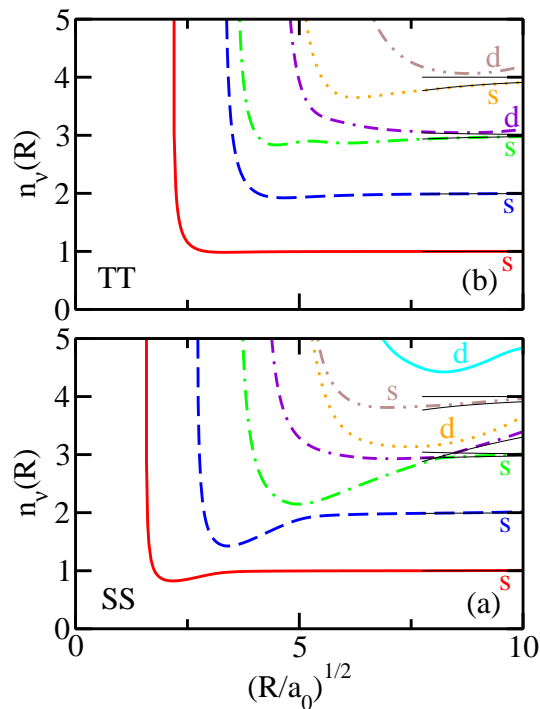


FIG. 1: (Color online) Adiabatic potential curves for $L^\pi = 0^+$ and charge conjugation eigenvalue $+1$ shown as effective quantum numbers [see Eq. (14)] vs \sqrt{R} . Panels (a) and (b) are for $(S_+, S_-) = (0, 0)$ and $(1, 1)$, respectively. The thin solid lines show the known asymptotic behavior through order R^{-3} . The asymptotically ionic channel in (a) is the dash-dash-dotted line. The dimer-dimer asymptotic thresholds are labeled by the angular momentum of the excited Ps.

III. ADIABATIC POTENTIAL CURVES

This paper is concerned with states of $L = 0$ angular momentum and positive parity π . Our matrix element calculations utilize a technique that reduces all matrix element evaluations to 1-D Fourier transforms [13]. Using this basis, the lowest few adiabatic potentials are calculated for the $2e^-2e^+$ system and shown in Figs. 1 and 2. To put all adiabatic potentials on the same scale, the curves are plotted as effective quantum numbers $n_\nu(R)$ [6, 8] as functions of the square root of the hyperradius R . This scaling is motivated by the fact that, at low energy, all curves except the asymptotically ionic channel break up into two Ps dimers at large hyperradius. At the low energies considered here, one of these Ps dimers is always in the ground state in the asymptotic limit. Thus, based on the asymptotic thresholds energies, we define

$$n_\nu(R) = [-4U_\nu(R)/E_H - 1]^{-1/2} \quad (14)$$

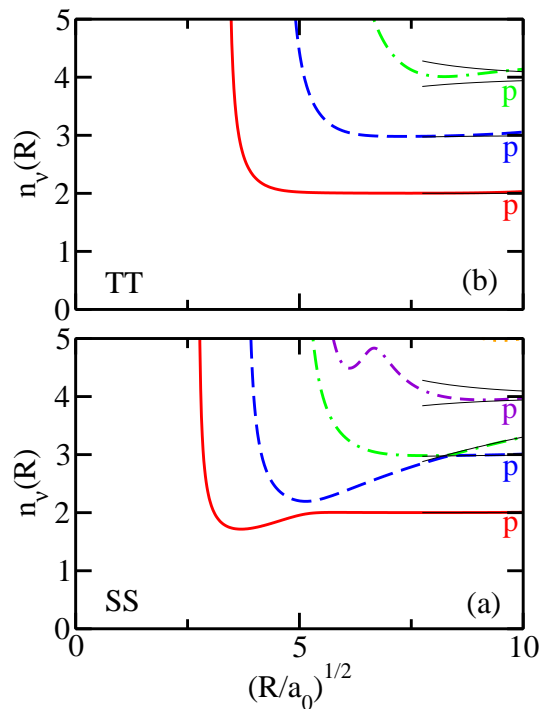


FIG. 2: (Color online) Adiabatic potential curves for $L^\pi = 0^+$ and charge conjugation eigenvalue -1 shown as effective quantum numbers vs \sqrt{R} . Panels (a) and (b) are for $(S_+, S_-) = (0, 0)$ and $(1, 1)$, respectively. The thin solid lines show the known asymptotic behavior through order R^{-3} . The asymptotically ionic channel in (a) is the dash-dotted line. The dimer-dimer asymptotic thresholds are labeled by the angular momentum of the excited Ps.

Figure 1 shows the eigenstates of \hat{C} corresponding to eigenvalue $+1$ for (a) the SS and (b) the TT spin configurations. In general, the potentials of the TT case are more repulsive since the Pauli exclusion principle keeps the identical particles further apart. Moreover, only in the SS case does the ionic channel appear. In a diabatic picture, this ionic channel, with threshold energy $-0.262E_H$ [$n_\nu(\infty) = 4.56$], crosses dimer-dimer channels with $n_\nu(\infty) \leq 4$, each crossing becoming less sharp (less diabatic) for crossings at lower energy.

Figure 2 shows the eigenstates of \hat{C} corresponding to eigenvalue -1 for (a) the SS and (b) the TT spin configurations. Again, we observe the potentials of the TT case are more repulsive than the potentials of the SS spin configuration. Panel (a) shows the diabatic-like ionic channel, which is absent in panel (b). Moreover, the dash-dash-dotted line of panel (a) has a local minimum around $\sqrt{R/a_0} \approx 6.5$. Though not visible on the scale shown, this is due to an avoided crossing with the next highest channel. Though the curves begin to be less converged

in this region, it is a true feature and not an artifact. Taking into account the other adiabatic potentials (not shown), even though unconverged, they hint that this is just the first of many avoided crossings at large R and appear to map out a diabatic curve that asymptotically approaches $-0.25E_H$, that is, the energy where one dimer has completely dissociated.

The asymptotic limits up through order R^{-3} are shown as thin solid lines at large R in both Figs. 1 and 2. This asymptotic behavior can be calculated by asymptotically expanding the adiabatic Hamiltonian in powers of R^{-1} [24] and using degenerate perturbation theory. This yields, for the dimer-dimer channels shown,

$$U_\nu(R \rightarrow \infty) \approx \frac{-1}{4} + \frac{-1}{4n^2} + \frac{1}{4\mu R^2} \left[3l(l+1) - n^2 - 2 - \frac{2^8 n^5 \delta_{l0}}{(n^2 - 1)^4} \left(\frac{n-1}{n+1} \right)^{2n} \right] + \frac{1}{3\mu^{3/2} R^3} \frac{2^{11} n^7 \delta_{l1}}{(n^2 - 1)^5} \left(\frac{n-1}{n+1} \right)^{2n}, \quad (15)$$

where the two terms involving Kronecker deltas only contribute if $n > 1$.

The number of asymptotic channels can be understood by examining the asymptotic wave functions [24]. For the dimer-dimer thresholds, ignoring the spin part of the wave function, the unsymmetrized asymptotic wave function is effectively a product of two scaled hydrogenic radial wave functions and a coupled set of spherical harmonics whose angles are defined by the Jacobi vectors ρ_j ,

$$|\Phi(R \rightarrow \infty)\rangle \approx |n_1 l_1\rangle_1 |n_2 l_2\rangle_2 |\hat{\rho}_1 \hat{\rho}_2 \hat{\rho}_3\rangle, \quad (16)$$

where $|nl\rangle_j$ represent the hydrogenic wave function along the j th Jacobi vector and

$$|\hat{\rho}_1 \hat{\rho}_2 \hat{\rho}_3\rangle = \frac{(-1)^{l_3}}{\sqrt{2l_3 + 1}} \sum_{\mathbf{m}} \langle l_1 m_1 l_2 m_2 | l_3 m_3 \rangle \times Y_{l_1 m_1}(\hat{\rho}_1) Y_{l_2 m_2}(\hat{\rho}_2) Y_{l_3 m_3}^*(\hat{\rho}_3). \quad (17)$$

The sum is over all projection quantum numbers, Y are spherical harmonics, and $\langle \cdot \rangle$ is a Clebsch-Gordan coefficient.

The Jacobi vector ρ_1 defines the first dimer, ρ_2 defines the second dimer, and ρ_3 defines the inter-dimer distance. Applying the symmetrization operator \hat{S} yields

$$\hat{S}|\Phi(R \rightarrow \infty)\rangle \approx |n_1 l_1\rangle_1 |n_2 l_2\rangle_2 |\hat{\rho}_1 \hat{\rho}_2 \hat{\rho}_3\rangle + (-1)^{l_3} |n_2 l_2\rangle_1 |n_1 l_1\rangle_2 |\hat{\rho}_2 \hat{\rho}_1 \hat{\rho}_3\rangle \quad (18)$$

since the terms arising from P_{12} and P_{34} are exponentially negligible. This can be understood since, if expressed in a single Jacobi basis, these operators cause the Jacobi vectors to pick up components along ρ_3 . In the asymptotic limit, ρ_3 scales with the hyperradius R and thus the hydrogenic wave function causes the exchange term to vanish exponentially. The functions Eq. (18) are

eigenstates of the charge conjugation projection operator \hat{C}_\pm ,

$$\hat{C}_\pm \hat{S}|\Phi(R \rightarrow \infty)\rangle = [1 \pm (-1)^{l_1 + l_2}] \hat{S}|\Phi(R \rightarrow \infty)\rangle. \quad (19)$$

If one dimer is in the ground state, then the asymptotic wave function vanishes for \hat{C}_+ if the other dimer is in an odd partial wave. On the other hand, the asymptotic wave function vanishes for \hat{C}_- if the other dimer is in an even partial wave.

In this way, in a diabatic picture the adiabatic potentials can be labeled by how they approach the asymptotic thresholds (shown as thin solid lines at large R). In Fig. 1(b), for example, solid, dashed, dash-dotted, dash-dash-dotted, dotted, and dash-dot-dotted lines are for $1s1s$, $1s2s$, $1s3s$, $1s3d$, $1s4s$, and $1s4d$ Ps-Ps channels, respectively. In Fig. 1(a), the labeling is shifted due to the inclusion of the ionic channel, such that the ionic channel is the dash-dash-dotted line while solid, dashed, dash-dotted, dotted, dash-dot-dotted, and solid lines are for $1s1s$, $1s2s$, $1s3s$, $1s3d$, $1s4s$, and $1s4d$ Ps-Ps channels, respectively. In Fig. 2(b), solid, dashed, and dash-dotted lines are for $1s2p$, $1s3p$, and $1s4p$ Ps-Ps channels, respectively. In Fig. 2(a), the labeling is shifted due to the inclusion of the ionic channel, such that the ionic channel is the dash-dotted line while solid, dashed, and dash-dash-dotted lines are for $1s2p$, $1s3p$, and $1s4p$ Ps-Ps channels, respectively.

Our current scheme suffers from convergence issues in the asymptotically large R region for states other than s -wave. This is visible in the dotted and upper solid lines of Fig. 1(a), the dash-dash-dotted and dash-dot-dotted lines of Fig. 1(b), as well as the dash-dotted line of Fig. 2(b). Even more, the potentials that asymptotically approach the $1s4f$ threshold in Fig. 2 are even less converged, not appearing within the figure on the scale shown. In practice, the adiabatic potentials are smoothly matched to the known asymptotic behavior.

IV. LOW ENERGY ELASTIC SCATTERING

This section describes the low energy elastic scattering properties for those systems shown in Fig. 1, that is, the s -wave scattering lengths for the TT and SS spin configurations. The inverse log-derivative R -matrix is propagated from small hyperradius out to some matching distance R_m , where it is matched to the asymptotic form of the hyperspherical wave functions. For short-range interaction potentials, the couplings and adiabatic potentials fall off sufficiently fast such that a sufficiently large matching point R_m leads to converged results. For the long-range Coulomb interaction, however, we find it better to match the R -matrix at many different points and then extrapolate to infinite matching point.

As an example, Fig. 3 shows the tangent of the s -wave phase shift as a function of the inverse of the match-

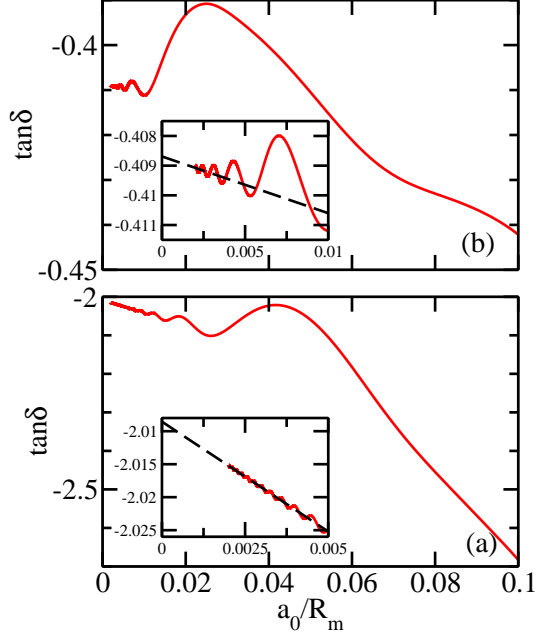


FIG. 3: (Color online) Tangent of the phase shift δ as a function of the matching distance R_m for low-energy elastic scattering of the $(S_+, S_-) = (0, 0)$, $L^\pi = 0^+$ system using the four lowest channels. Panels (a) and (b) are for a scattering energies of $E_{\text{scatt}} = 0.01 E_H$ and $0.001 E_H$, respectively. The dashed line of the insets shows a linear fit over $a_0/R_m = 0 - 0.003$.

ing point for the SS system. The TT system is qualitatively similar. Panel (a) is for a scattering energy $E_{\text{scatt}} = 0.01 E_H$ above the $1s1s$ threshold, while panel (b) is for a scattering energy $E_{\text{scatt}} = 0.001 E_H$. The oscillations in $\tan \delta$ as a function of R_m begin at $R \approx 25 a_0$, that is, beyond the distance where there is an appreciable potential well. However, it is the long-range nonadiabatic coupling, which between s -wave dimer-dimer states goes as $P_{\nu\nu'}(R \rightarrow \infty) \approx R^{-1}$ at large distance, that leads to the oscillating behavior. This has been verified by artificially turning off these couplings beyond some large distance and observing that the oscillations cease.

In addition to the oscillating behavior, $\tan \delta$ approaches the infinite matching point linearly when plotted as a function of R_m^{-1} . In practice, we fit to this linear behavior, making the range of the fit extend over many wavelengths to average out the oscillations. The insets of Fig. 3 show such fits. The oscillations have a smaller wavelength as the scattering energy increases, such that the fits to the $\tan \delta$ with the lowest scattering energy have a larger uncertainty.

Figure 4 shows the energy-dependent s -wave scattering lengths, $a = -\tan \delta/k$, where k is the scattering momentum, as a function of the scattering energy E_{scatt} , where

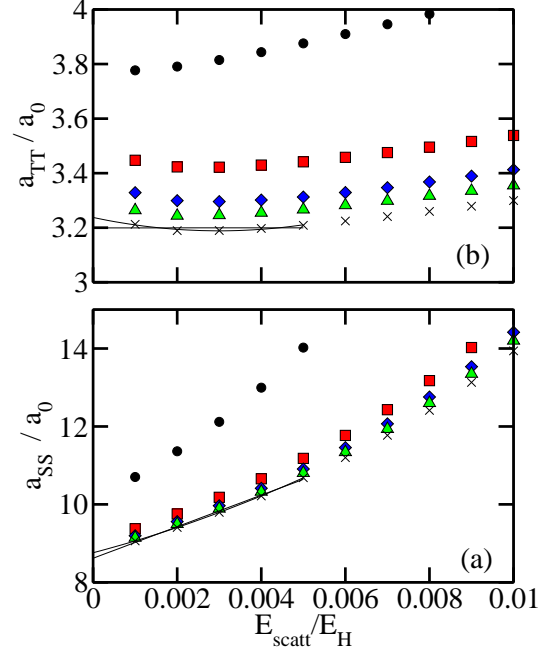


FIG. 4: (Color online) Low-energy s -wave scattering length a vs scattering energy E_{scatt} for (a) the SS configuration and (b) the TT configuration. Circles, squares, diamonds, and triangles are for 1–4 included channels, respectively. Crosses represent extrapolating to infinite number of channels, based on the data for 2–4 included channels. Upper and lower thin solid lines are quadratic and linear fits, respectively, of the extrapolated data.

E_{scatt} is the energy above the lowest dimer-dimer threshold of $-0.5 E_H$. Circles, squares, diamonds, and triangles show the SS s -wave scattering length a_{SS} including one, two, three, or four lowest channels. The crosses are an extrapolation to an infinite number of channels based on the data for including the lowest two through four channels. The thin lines show linear and quadratic fits to the extrapolated data set using the five points of lowest scattering energy. In Fig. 4(b), a similar analysis is done for the TT scattering length a_{TT} . The analysis estimates the scattering lengths to be $a_{\text{SS}} = 8.7(2)a_0$ and $a_{\text{TT}} = 3.2(1)a_0$.

The scattering estimates provided agree well with others (see Table II), but are systematically large when compared to the accurate stochastic variational method [33, 34]. This systematic error at low scattering energy arises from a number of sources. As already mentioned, the oscillations in $\tan \delta$ obscure the underlying linear behavior if the R -matrix is not propagated to sufficiently large distance. The more probable cause is that at low scattering energy the scattering data is very sensitive to small changes in the realistic potentials, that is, the adiabatic potentials $U_\nu(R)$ with diagonal $Q_{\nu\nu}(R)$ correction. In

TABLE II: The s -wave scattering length in atomic units for some calculations of Ps-Ps scattering.

Method	Singlet	Triplet
CCA [28] ^a	7.46	1.56
CCA [29] ^b	9.32	2.95
HECG (present) [*]	8.7(2)	3.2(1)
Oda <i>et al.</i> [30] ^c	8.26	3.02
Platzmann and Mills [17]	≈ 5.7	≈ 1.9
QMC [31] ^d	9.148(42)	3.024(58)
QMC [32] ^e	$\gtrsim 9.148(42)$	2.900(34)
Superseded SVM [33, 34] ^f	8.443	2.998

^a For basis set Ps(1s)Ps(1s, 2s, 2p).

^b For basis set Ps(1s, 2s, 2 \bar{p} , 3 \bar{d}) Ps(1s, 2s, 2 \bar{p} , 3 \bar{d}); bar denotes pseudostate.

^c Model: long-range van der Waals potential with short-range hard core, constrained to fit Ps₂ binding energy.

^d Polynomial fit to phase shift.

^e Same data as [31], but fit to effective range theory. Singlet value unknown, but deduced to be slightly larger than in [31].

^f Error bars beyond digits shown.

^{*} See text for the description of the error estimate.

practice, where possible, an inverse power-law fit is performed on the large- R tails of the realistic potentials as this matches the expected behavior at large distance. However, in some cases a nonadiabatic coupling occurs in the region where the inverse power-law asymptotics would be expected, obscuring this behavior. Thus, instead of a power-law fit, we find a Lorentzian-like tail to be a more appropriate large R fit to the realistic potential. Nevertheless, since the realistic potentials are a variational upper bound to the true potentials, the scattering data at low scattering energy is systematically higher than expected. A fit of the zero-energy s -wave scattering lengths using the scattering data at higher energy would provide an estimate much closer to accepted values, but is not provided here.

We estimate the error by fitting the N -channel scattering data to quadratic and linear polynomials, extrapolating to zero scattering energy. An example is shown in Fig. 4 for the infinite channel approximation (crosses). This provides error estimates for each fixed-channel calculation. The difference between the 4-channel calculation and infinite-channel approximation are used to then estimate an overall error.

The scattering lengths reported in Table II are not the experimentally relevant scattering lengths. Those reported are for the singlet-singlet or triplet-triplet symmetries of the identical electrons and positons. For experiment, it is the spin of the Ps atoms that is relevant. It is a straightforward calculation to switch between the two coupling schemes; see, e.g. Refs. [32] or [34].

V. CHARGE REDISTRIBUTION

This section describes the charge redistribution, that is, the probability of transferring from a dimer-dimer channel to the ionic channel that occurs in only the systems with SS symmetry. The probabilities are given by the squared absolute value of the S -matrix elements. The S -matrix is calculated after propagating the R -matrix to a large distance. Similar to the approach shown in Fig. 3, each element of the S -matrix is extrapolated to matching to the asymptotic solutions at $R \rightarrow \infty$.

In the following, for positive charge conjugation symmetry, only the lowest four channels are included in the calculations [the solid, dashed, dash-dotted, and dash-dash-dotted lines of Fig. 1(a)]. The dimer-dimer channels fragment into one ground state s -wave Ps and one excited state s -wave Ps. No d -wave [dotted and upper solid lines of Fig. 1(a)] or the highest s -wave [dash-dot-dotted line of Fig. 1(a)] fragmentation channels are included. Beyond the crossing with the third dimer-dimer channel, the ionic channel is made continuous up to the ionic threshold of $-0.262E_H$, where all crossings with the neglected dimer-dimer channels are assumed to be fully diabatic. For the negative charge conjugation symmetry, only the lowest three channels are included in the calculations [the solid, dashed, and dash-dotted lines of Fig. 2(a)]. The asymptotically dimer-dimer channels fragment into one ground state s -wave Ps and one excited state p -wave Ps. No f -wave [not shown in Fig. 2(a)] or the highest p -wave [dash-dash-dotted line of Fig. 2(a)] fragmentation channels are included. Beyond the crossing with the second dimer-dimer channel, the ionic channel is made continuous up to the ionic threshold of $-0.262E_H$, where all crossings with the neglected dimer-dimer channels are assumed to be fully diabatic.

Figure 5 shows some of the squared absolute values of the off-diagonal S -matrix elements for the SS system with (a) positive and (b) negative charge conjugation symmetry. In panel (a), solid ($|S_{14}|^2$), dashed ($|S_{24}|^2$), and dash-dotted ($|S_{34}|^2$) lines show the transition probabilities to transition from the three lowest dimer-dimer channels to the ionic channel. The charge transfer is most efficient from the ground dimer-dimer channel and is less efficient as the excited Ps increases in principle quantum number. This can be understood since the avoided crossing is largest between the ground and first excited states. Thus, any flux coming in on the ground state is efficiently transferred to the higher channels as opposed to simply exciting one of the Ps atoms, whereas flux coming in on the first excited state is more efficiently given to the ground state rather than transferring to the ionic channel. The crossing of the third dimer-dimer channel is almost fully diabatic, hence there is no efficient charge transfer from this state to the state of the Ps ion and a free charge. This trend of the crossings becoming more diabatic as the energy increases supports our approach of neglecting the more excited dimer-dimer channels.

In Fig. 5(b), solid ($|S_{13}|^2$) and dashed ($|S_{23}|^2$) lines

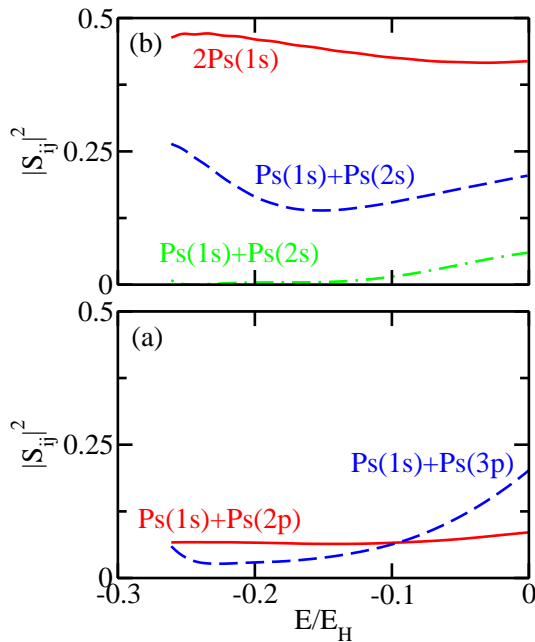


FIG. 5: (Color online) Charge redistribution probabilities as a function of scattering energy for SS and (a) positive or (b) negative charge conjugation symmetry. All curves are for dimer-dimer to ionic transitions and are labeled by the dimer-dimer threshold. The ionic threshold is $-0.262E_H$.

show the transition probabilities to transition from the two lowest dimer-dimer channels to the ionic channel. Overall, the charge transfer is not as efficient in comparison to the case of positive charge conjugation symmetry. This can be understood since there is only one wide avoided crossing, but it is not as wide as in the case of positive charge conjugation symmetry. The second curve crossing is already mostly diabatic, suppressing much of the probability to transfer to the ionic channel.

VI. CONCLUSION AND OUTLOOK

This paper calculates the lowest adiabatic potential curves as a function of the hyperradius R for the $2e^+2e^-$

system for zero orbital angular momentum, positive parity, and different charge conjugation symmetries. Using these hyperradial channels, low-energy elastic scattering properties are determined by propagating the R -matrix. The long-range couplings from the Coulomb interactions are overcome by matching to the asymptotic hyperradial functions at many different points. The observed behavior in the tangent of the phase shift and the calculated S -matrix elements, as a function of inverse matching point, is linear with damping oscillations. The resulting s -wave scattering lengths are larger than other values in the literature, but nevertheless converge well as a function of the number of included channels and provide reasonable estimates of the scattering properties. The transition probabilities are expected to be good estimates, but could be improved by including more channels.

The ability to treat the ionic and dimer-dimer fragmentation channels on an equal footing is one of the strengths of the adiabatic hyperspherical method. Future studies will extend this system to include inelastic scattering properties and different orbital angular momentum states. Moreover, the masses and charges of the particles are tunable parameters. It would be interesting to study e.g. the change in the potential curves and transition amplitudes as a function of the mass of the positive charge transitioning from the Ps_2 to the H_2 system. Explicitly including hydrogenic wave functions in the basis could also help the convergence issues at large hyperradius. These topics will be the focus of future studies.

VII. ACKNOWLEDGEMENTS

Support by the National Science Foundation through Grant No. PHY-1306905 and by the US Department of Energy, Office of Science through Grant No. DE-SC0010545 is gratefully acknowledged.

-
- [1] J. Macek, J. Phys. B **1**, 831 (1968).
 - [2] C. D. Lin, Phys. Rev. A **10**, 1986 (1974).
 - [3] J. Botero and C. H. Greene, Phys. Rev. Lett. **56**, 1366 (1986).
 - [4] J. Macek and K. A. Jerjian, Phys. Rev. A **33**, 233 (1986).
 - [5] V. V. Gusev, V. I. Puzynin, V. V. Kostykin, A. A. Kvitsinsky, S. P. Merkuriev, and L. I. Ponomarev, Few-Body Systems **9**, 137 (1990).
 - [6] H. R. Sadeghpour and C. H. Greene, Phys. Rev. Lett. **65**, 313 (1990).
 - [7] B. J. Archer, G. A. Parker, and R. T. Pack, Phys. Rev. A **41**, 1303 (1990).
 - [8] B. D. Esry and H. R. Sadeghpour, Phys. Rev. A **67**, 012704 (2003).
 - [9] C. D. Lin, Phys. Rep. **257**, 1 (1995).
 - [10] S. Watanabe, Phys. Rev. A **25**, 2074 (1982).

- [11] T. Morishita and C. D. Lin, Phys. Rev. A **57** 4268 (1998).
- [12] J. P. D’Incao, Phys. Rev. A **67**, 024501 (2003).
- [13] K. M. Daily and C. H. Greene, Phys. Rev. A **89**, 012503 (2014).
- [14] K. Hagiwara *et al.* (Particle Data Group), Phys. Rev. D, **66**, 010001(R) (2002).
- [15] G. Weidenspointner, *et. al*, Astron. and Astrophys. **450**, 1013 (2006).
- [16] G. B. Andresen, *et. al*, Nat. Lett. , 09610 (2006).
- [17] P. M. Platzman and A. P. Mills, Jr., Phys. Rev. B **49**, 454 (1994).
- [18] A. P. Mills, Jr., Nucl. Instr. Meth. Phys. Res. B **192**, 107 (2002).
- [19] D. B. Cassidy, S. H. M. Deng, R. G. Greaves, T. Maruo, N. Nishiyama, J. B. Snyder, H. K. M. Tanaka, and A. P. Mills, Jr., Phys. Rev. Lett. **95**, 195006 (2005).
- [20] H. K. Avetissian, A. K. Avetissian, and G. F. Mkrtchian, Phys. Rev. Lett. **113** 023904 (2014).
- [21] Y.-H. Wang, B. M. Anderson, and C. W. Clark, submitted to Phys. Rev. A, arXiv:1402.5159 (2014).
- [22] D. B. Cassidy and A. P. Mills, Jr., Nature **449**, 195 (2007).
- [23] S. T. Rittenhouse, J. von Stecher, J. P. D’Incao, N. P. Mehta, and C. H. Greene, J. Phys. B **44**, 172001 (2011).
- [24] K. M. Daily, submitted to Phys. Rev. A (2014).
- [25] J. von Stecher and C. H. Greene, Phys. Rev. A **80**, 022504 (2009).
- [26] D. Rakshit and D. Blume, Phys. Rev. A **86** 062513 (2012).
- [27] J. Mitroy, S. Bubin, W. Horiuchi, Y. Suzuki, L. Adamowicz, W. Cencek, K. Szalewicz, J. Komasa, D. Blume, and K. Varga, Rev. Mod. Phys. **85**, 693 (2013).
- [28] S. K. Adhikari, Phys. Lett. A **294**, 308 (2002).
- [29] S. Chakraborty, A. Basu, and A. S. Ghosh, Nucl. Instr. Meth. Phys. Res. B **221** 112, (2004).
- [30] K. Oda, T. Miyakawa, H. Yabu, and T. Suzuki, J. Phys. Soc. Jpn. **70**, 1549 (2000).
- [31] J. Shumway and D. M. Ceperley, Phys. Rev. B **63**, 165209 (2001).
- [32] J. Shumway and D. M. Ceperley, Solid State Commun. **134**, 19 (2005).
- [33] I. A. Ivanov, J. Mitroy, and K. Varga, Phys. Rev. Lett. **87**, 063201 (2001).
- [34] I. A. Ivanov, J. Mitroy, and K. Varga, Phys. Rev. A **65**, 022704 (2002).